On the conversion of NDP Energy Spectra into Depth Concentration Profiles for Thin-Films All-Solid-State Batteries

A three-step numerical procedure has been developed, which facilitates the conversion of NDP energy spectra into lithium concentration depth profiles for thin-film Li-ion batteries. The procedure is based on Monte Carlo modeling of the energy loss of charged particles (ions) in the solid media, using the publically available SRIM/TRIM software. For the energy-to-depth conversion, the battery stack has been split into finite volume elements. Each finite volume element becomes a source of ions according to the employed nuclear reaction. Ions loos energy when they move across the battery stack towards the detector. The as-obtained simulated spectra have been compared with the experimentally measured spectra. The thicknesses of the battery stack layers were estimated by minimizing the deviation between the simulated and measured spectra. Subsequently, a relation between the average energy of detected ions and the depth of the corresponding finite volume element, yielding a calibration function, was used to relate that particular part of the spectra with the depth of its source. At the final stage, a Bayesian estimator was used to find the distribution of lithium at a particular depth. The developed procedure was applied to a practically relevant case study of Si immobilization in the LPO electrolyte of all-solid-state thin-film batteries. It is shown that the lithium immobilization process in the LPO electrolyte is responsible for the battery degradation process.

Keywords: thin-film battery, all-solid-state battery, NDP, aging

1. Introduction

In recent years our society more and more use renewable electricity. Wind, solar and hydropower slowly but steadily replace fossil fuels [1-2]. However many renewable energy sources also suffer from irregularity in supply, which unavoidably demands electricity storage in various forms. Li-ion batteries (LIB) quickly become the workhorse of numerous portable, mobile, and stationary storage appliances. Such devices have high energy density, low self-discharge, and reasonably long service life. However, they are sensitive to extremely low and high temperatures and may burn or even explode in over(dis)charge situations. One of the perspective ways to improve the safety of Li-ion batteries is to replace the inflammable liquid electrolyte by a solid-state ceramic, leading to all-solid-state batteries. Nowadays all-solid-state Li-ion batteries with Si anode are quickly gaining popularity as a prospective research topic. The basic electrochemical charge transfer reactions of such a solid-state battery, using $LiCoO_2$ as cathode and Si as anode, can be represented by

$$\mathrm{LiCoO_2} \underset{\text{discharge}}{\overset{\text{charge}}{\rightleftarrows}} \mathrm{Li_{1-x}CoO_2} + x\mathrm{Li^+} + xe^-, \tag{1}$$

$$\mathrm{Si} + y\mathrm{Li^+} + ye^- \underset{\text{discharge}}{\overset{\text{charge}}{\rightleftarrows}} \mathrm{Li}_y\mathrm{Si}, \tag{2}$$

where $LiCoO_2$ can be reversibly cycled down to x = 0.47-0.5 and Si up to y = 3.75.

The performance of all-solid-state batteries with Si anode has been investigated by a number of *in situ* characterization methods [3], each having their own advantages and limitations. A neutron depth profiling (NDP) is a well-known method developed in the early 70s, to measure the depth distribution of various elements [4-8]. Recently NDP had been applied to the determination of lithium concentration gradients in electrochromic devices, [9-11] thin-film battery electrodes and electrolytes [12]. Applying NDP to LIB is based on the reaction of thermal neutrons with ^{6}Li. Low-energy (about 25 meV) neutrons interact with nuclei of ^{6}Li isotope causing the formation of α-particles (^{4}He) and tritons (^{3}H), according to

$$n + {}^6\mathrm{Li} \rightarrow {}^4\mathrm{He} + {}^3\mathrm{H}. \tag{3}$$

When locally generated, both ^{4}He and ^{3}H particles have well-defined energies of 2055 and 2727 keV, respectively [13-15]. However, while moving through the various battery materials the ^{4}He and ^{3}H particles will lose some energy. The energy of the outgoing particles can be estimated by detectors. A mathematical relationship between

the particles formation depth and energy loss can be established, allowing to *in situ* determine lithium concentration profiles. Depth profiles estimated by the NDP method are essential for understanding processes, occurring in layers of battery stacks [16-17].

2. Basics of energy loss theory

Eq. 3 describes the formation of two types of charged particles (ions), the alpha particles (^{4}He) and tritons (^{3}H) with an initial energy of 2.055 and 2.727 MeV, respectively. On the way to the sample surface, the charged particles are losing energy proportional to the distance of their pathways in the solid materials. The resulting energy spectra of both particles can be measured for further analysis.

Fig. 1 presents several important characteristics of the energy loss of charged particles for a range of materials used in the production of thin-film batteries (simulations done by SRIM [18]). Fig. 1a and b illustrate the dependence of the energy of an alpha particle and tritons on its pathway (penetration depth). In general, the longer the pathway the more energy (E) is lost by both particles. The stopping power (S [MeV/μm]) is defined as the derivative of the energy (loss) with respect to traveling distance (x) in the given material, according to

$$S = -\frac{dE}{dx} \quad . \tag{4}$$

According to the original work of Bohr [19,20] the stopping power of the charged particle in the solid media is composed of two terms. The first term is caused by the interaction of the incoming ions with the electronic clouds of the material atoms. This component is dominant for the battery materials under consideration and ion energies relevant to this paper. The second component is attributed to interactions of the ions with the nuclei of the materials. From Fig. 1c and d it can be concluded that this contribution is much smaller and can be neglected in computational simulations. Fig. 1c and d also shows the significant difference in magnitudes between the electronic (solid curves) and nuclear (dashed curve) stopping power for alpha particles and tritons in the same materials as in Fig. 1a and b. Obviously, the stopping power strongly depends on the energy and, therefore, on the traveling distance. Fig. 1e and f show the stopping power of alpha particles and tritons,

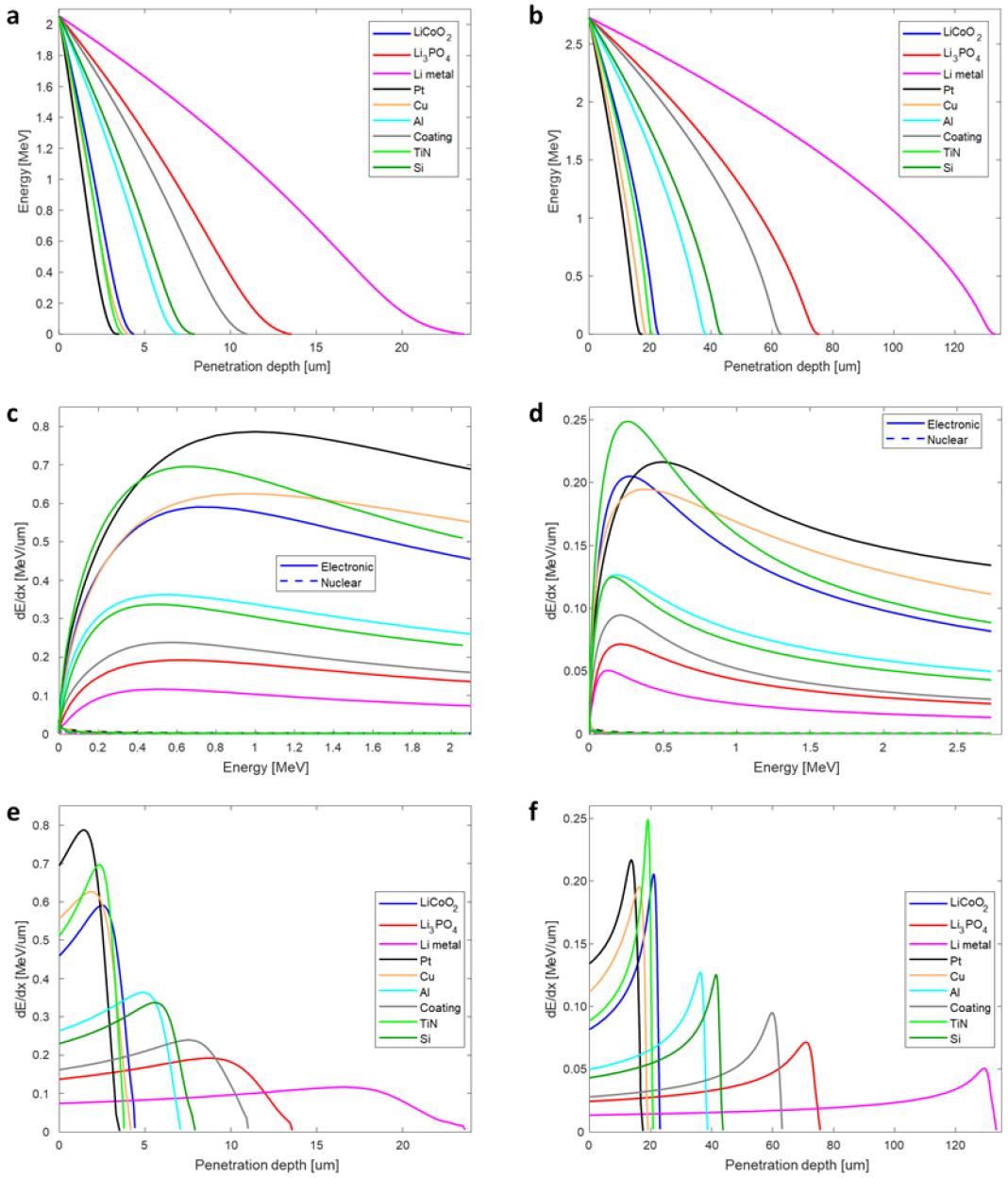

Fig. 1. Relation between the energy of an ion and the traveled distance inside various battery materials for alpha (a) and triton particles (b). Electronic (solid lines) and nuclear (dashed lines) contributions of the stopping power for α-particles and tritons in various materials (c) and (d), accordingly. Corresponding Bragg curves of alpha particles (e) and tritons (f).

accordingly, as a function of the penetration depth for the same materials as shown in the previous figures. It can be seen that for each material the stopping power reaches a maximum, named a Bragg peak, and then quickly declines when the particles slow down to zero speed. Both stopping power and penetration depth strongly depend on the type of target material. From Fig. 1a, c and e it can be seen, that for the alpha particles platinum

has the largest stopping power of about 0.8 MeV/μm (at the peak) and the smallest maximal penetration depth of approximately 3.5 μm, while light-weight Li metal combines the smallest stopping power of 0.1 MeV/μm with the largest penetration depth of 23.5 μm. A general tendency can be observed, that materials containing lighter elements have smaller stopping power and reveal larger penetration depth. From Fig. 1b, d and f it can be concluded that a similar tendency also holds for tritons. It also can be observed that lighter and faster tritons have considerably smaller stopping power, and therefore demonstrate much larger penetration depth, which can reach up to 133 μm for metallic lithium and 17.5 μm for platinum. Such a strong variation in stopping power for different ions and materials requires a theoretical explanation.

The following plain and intuitive derivations reproduce the historically first equation, describing the stopping power. Consider an ion with atomic number Z_1 moving with speed v inside a (target) material with atomic number Z_2 and atomic weight M_2. The modern theoretical derivation of the stopping power is a refinement and extension of the original Bohr ideas and can be found in works of Bethe [21, 22] and Bloch [23, 24]. A general Bethe-Bloch stopping power expression has the following form

$$S = \frac{\kappa Z_2}{\gamma^2} Z_1^2 L(\gamma), \tag{5}$$

where $\gamma = v/c$ and c is the speed of light. The pre-factor κ follows the expression $\kappa = 4\pi r_0^2 m_e c^2$ in which m_e is the mass of an electron and $r_0 = e^2/(m_e c^2)$ is the Bohr electron radius. $L(\gamma)$ is called the stopping number, which has been expanded as

$$L(\gamma) = L_0(\gamma) + Z_1 L_1(\gamma) + Z_1^2 L_2(\gamma) + \cdots, \tag{6}$$

and describes all corrections for basic two-particle energy loss processes. $L_0(\gamma)$ corresponds to the original Fano formulation [25], the second term of the stopping number expansion $L_1(\gamma)$ is usually called Barkas correction (also called Z_1^3 correction), and the third term $L_2(\gamma)$ is called Bloch correction, or Z_1^4 correction. All those terms have an analytical form but are generally quite complicated. For example, the Fano formulation has been reported as

$$L_0(\gamma) = \frac{1}{2}\ln\left(\frac{2m_e c^2 \gamma^2 \Delta E_{max}}{1-\gamma^2}\right) - \gamma^2 - \frac{B}{Z_2} - \ln\langle I\rangle - \frac{\delta}{2} \tag{7}$$

where $\langle I\rangle$ is the mean ionization energy of the target atom, B/Z_2 is the shell correction term, $\delta/2$ is the density correction and ΔE_{max} is the largest possible energy loss in a single

collision with a free electron, given by

$$\Delta E_{max} = \left(\frac{2m_e c^2 \gamma^2}{1-\gamma^2}\right)\left(1 + \frac{2m_e}{M_1\sqrt{1-\gamma^2}} + \left[\frac{m_e}{M_1}\right]^2\right)^{-1} \quad (8)$$

The shell correction term $^{B}/_{Z_2}$ deals with the assumption that the velocity of the incoming ion is much larger than the velocities of electrons in the target materials. This term may contribute up to 10% of overall stopping power and is determined by the electronic structure of the host material. Various approximations are applied to calculate that term, such as hydrogenic wave functions, local density approximations or empirical corrections. The mean ionization energy ⟨I⟩ accounts for the discrete energy levels of the electrons in the target substance. As proposed by Fano, the shall correction term and the mean ionization energy can be treated as a combined term, which has been estimated from the experimentally measured electronic stopping power [26]. The density effect $^{\delta}/_{2}$ takes into account the polarization of the target material, which results in the reduction of the electromagnetic energy of the incoming ion in comparison with free-space values. Finally, it should be noted that classical Bethe-Bloch formalism lacks accuracy in the determination of stopping power for low-velocity situations. In that case, the incoming ion may capture target electron(s), which results in (partial) neutralization of its charge. Northcliff [27] introduced 'statistical net charge' correction to the charge of the partially neutralized ion, according to

$$\frac{Z_1^*}{Z_1} \equiv 1 \quad \exp\left(\frac{v}{v_0 Z_1^{2/3}}\right). \quad (9)$$

where v_0 is an electron orbital velocity. Eq. 9 is also a simplification and is known to underestimate this neutralization effect. It is known that in the low energy regions of 100-200 keV the deviation of Bethe-Bloch equation with experimental results can reach 15-25% [28]. An exhaustive overview of energy loss theory can be found in [29, 30].

3. Finite Volume Discretization

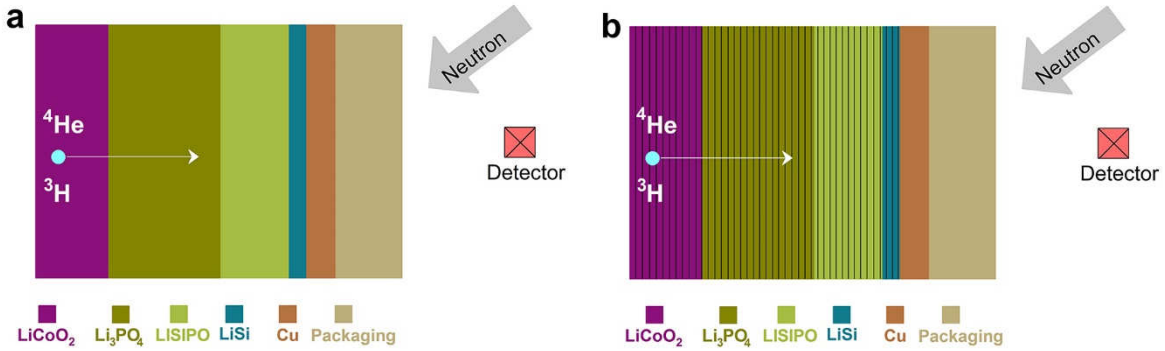

Fig. 2. Original battery stack (a). Layout of the finite volume discretization (b).

To model the NDP energy spectra of solid-state batteries, the layered structure of the battery stack is discretized into Finite Volume Elements (FVE), as schematically shown in Fig. 2. The original battery stack can be seen in Fig. 2a, and comprises of 6 layers of different composition. Note, that only lithium-containing parts of the stack can generate ions, therefore only those layers are discretized by FVE as shown in Fig. 2b. Denote the FVE number as i, which ranges from 1 to N and introduce the molar concentration [mol·cm^{-3}] of Li in the ith FVE, according to

$$c_i^n = \rho \frac{St(Li)}{M} \tag{10}$$

where ρ is the density of the materials [g·cm^{-3}], M is the molar mass of the material [g·mol^{-1}] and St(Li) is the stoichiometric lithium content in the material. For example, for $LiCoO_2$ with density ρ = 4.9 g·mol^{-1}, and M is 98 g·mol^{-1}, St(Li) is 1. It is generally accepted that the fraction of ^{6}Li in natural abundant Li is the same in all materials. The ^{6}Li concentrations (c_i^n) can therefore be further renormalized, according to

$$c_i = \frac{c_i^n}{\sum_{i=1}^{N} c_i^n \Delta w} \tag{11}$$

where Δw is the width of an individual FVE. Consequently, $\sum_{i=1}^{N} c_i^n \Delta w = 1$ and therefore c_i represents the relative weight of a given FVE, and a set of c_i represents the normalized distribution of Li within a complete battery stack.

It is assumed that each FVE emits particles independently of any other FVE. The intensity of this elementary source is proportional to c_i. The energy loss of ions during the passage across a material is considered to be a random process. This process can be simulated by the publically available SRIM/TRIM Monte-Carlo program (SRIM-

2008.04) [18]. For the battery sample shown in Fig. 2a a set of 100 independent trajectories of ^{4}He and ^{3}H ions was simulated by SRIM. It was assumed that a source of the ions is in the deepest FVE, the leftmost FVE in Fig. 2b.

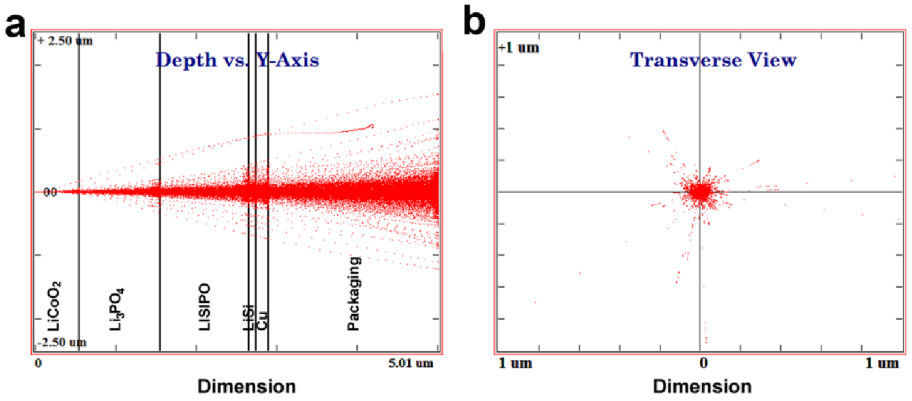

Fig. 3. Monte Carlo simulated trajectories of ^{4}He and ^{3}H ions moving through the entire battery stack (a). Transverse exit view where the ^{4}He and ^{3}H particles leave the battery stack surface, moving towards the detector (b).

Fig. 3 illustrates the basic functionality of SRIM. Fig. 3a shows the particle profile view, emitted from one of the inner FVE in the direction towards the outer interface. One clearly can see a spread in directions of ionic trajectories, which is minimal when just emitted but quite visible near the right edge of the battery stack. This spread is caused by the collision of heavy charged ions with atoms of the material. Fig. 3b illustrates a radial distribution of the exit points of ions at the surface, assuming a point source in the corresponding FVE in the depth.

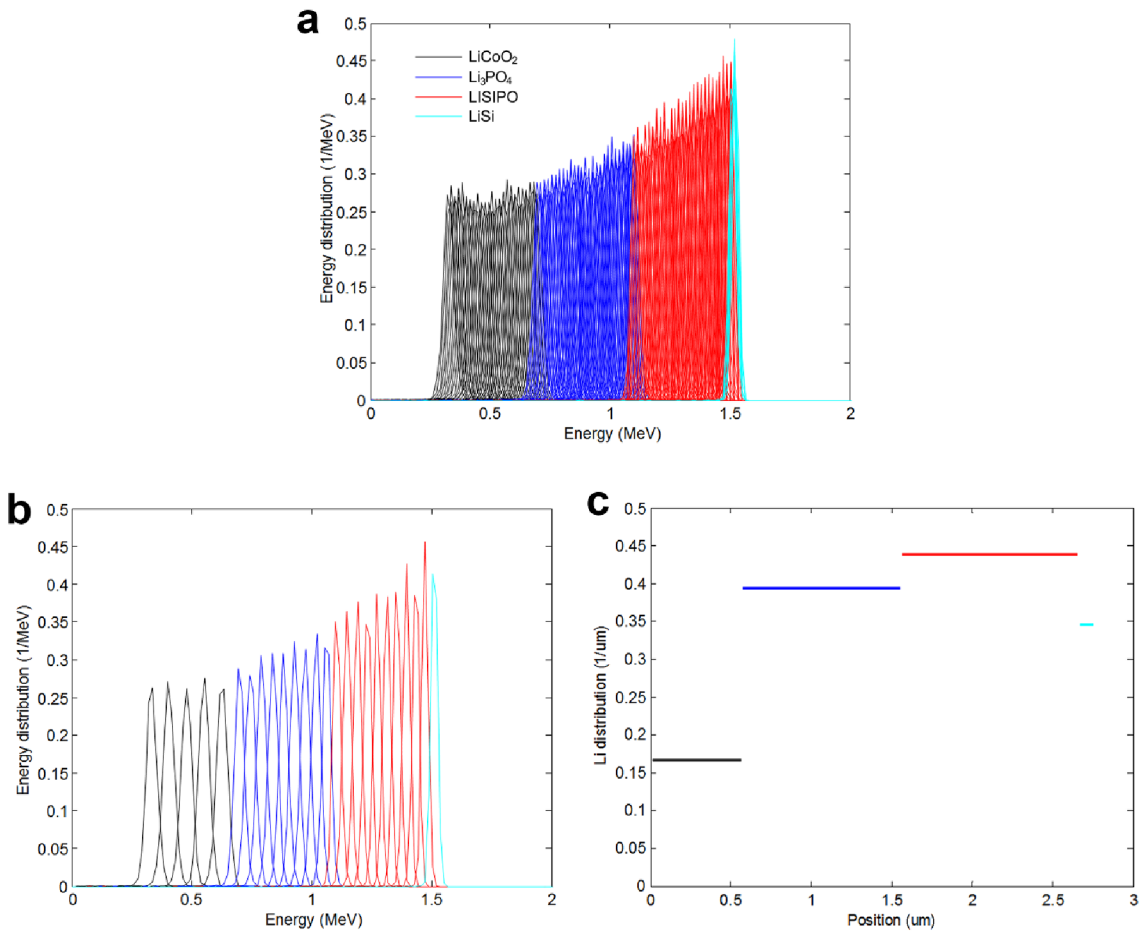

Fig. 4. Simulated energy distribution from 200 FEV elements (a). Spectra selected for each 8th element within the solid-state battery under investigation (b). Theoretically expected Li distribution inside the various thin film battery layers: $LiCoO_2$ (black line), LPO (blue), LiSiPO (red) and Si (cyan) (c).

The leftmost FVE in Fig. 2b will obviously result in particles with the lowest energy because those particles have to pass the longest distance through the material. The next FVE will give particles with somewhat larger energies and so on. The rightmost Li-containing FVE results in particles with the highest energy. Fig. 4 shows the simulated energy distributions from all 200 FVE (a) and from each 8th element (b) to better visualize the shape of energy distributions stemming from the individually selected FVE. It can be seen that the distance in energy distributions between signals of the individual FVE depends on the properties of the materials. Materials with larger stopping power, *e.g.* black curves for $LiCoO_2$, generate larger distances between the separate distributions than for example LPO (blue curves).

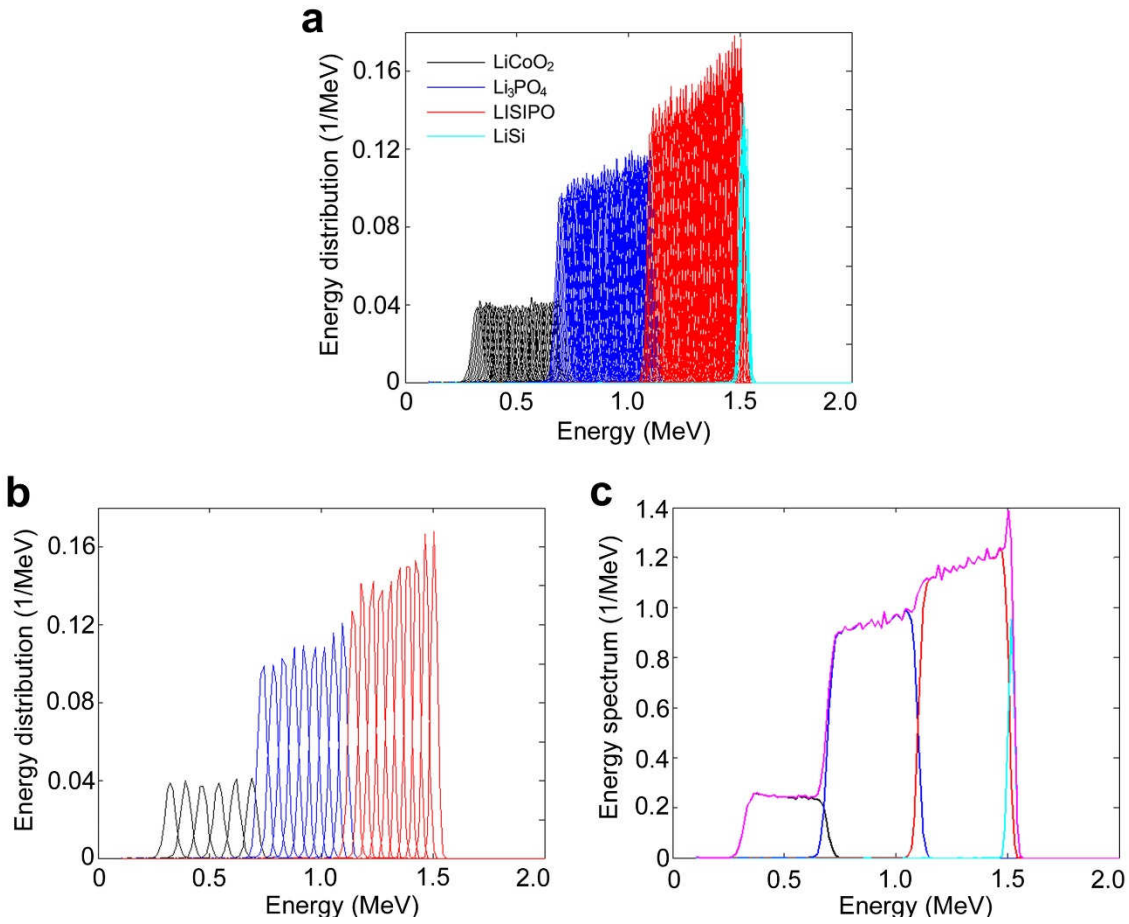

Fig. 5. Normalized simulated energy distributions from FEV for all elements (a). For clarity reasons the signals for each 8th element are shown (b) and resulting conversion into the energy spectrum (c).

The simulations shown in Fig. 4a presume that all FVE are identical and emit ions with equal intensity. In fact, the lithium content in FVE depends on the material, according to Eqs. 10 and 11. A theoretically expected normalized lithium concentration profile (Eq. 11) is shown in Fig. 4c. When the energy distributions depicted in Fig. 4a and b are normalized according to Fig. 4c, the resulting set of distributions are shown in Fig. 5a and b, illustrating how the total distribution looks like for a test cell. When the number of FVE increases, the contributions from individual FVE are more continuous and become less noisy. It is interesting to note that the energy contributions from the layers with high stopping power, such as $LiCoO_2$, produces lower average energies in the resulting spectrum because the corresponding part of the spectrum has a larger spread. In contrast, the layers with low stopping power (*e.g.* LPO) produce more compact peaks with higher average energy intensity. To obtain the total energy distribution, the contributions for the individual FVE must be added up. Fig. 5c was calculated by

summating contributions from all 200 FVE.

4. Determination of depth profiles

The main concern of the previous section was modeling of the energy distribution in the NDP experiments. That problem is interesting as it is, but also very important as a preliminary step in analyzing the lithium concentration profiles. The measured profiles are energy spectra and conversion into real lithium concentration profiles requires a method to reconstruct the lithium concentration at a particular depth on the basis of the energy signal. This section describes how such a depth profile algorithm can be set up.

The determination of the lithium concentration profiles is a three-step process. In the first step a set of preliminary estimated parameters of the sample, such as thicknesses of the layers, are fixed according to the manufacturing process. Then the molar lithium concentrations inside each layer are set according to the stoichiometry of the material. After that, the layer thicknesses are varied to obtain the best agreement between the theoretically calculated and experimentally observed energy spectra. Such procedure usually results in a reasonably good agreement with experimentally measured energy spectra as is shown in Fig. 6. The remaining deviations between calculations and experiment can be attributed to (local) deviations in the lithium concentration and can subsequently be estimated.

The estimation procedure is as follows. Denote a set of normalized concentrations in M separate FVE as $\mathbf{c} = (c_1, c_2, \dots, c_M)$. By definition, $\mathbf{c}$ is an M-dimensional vector. Denote the energy distribution (energy spectrum), *i.e.* the probability density function of energy, given the set of normalized lithium concentrations in each FVE as $f(e|\mathbf{c}) = f(e|c_1, \dots, c_M)$. Note that $f(e|\mathbf{c})$ is a conditional probability density function. Since the signals from separate FVE are considered to be independent, it follows that

$$f(e|c_1, \dots, c_M) = \sum_{j=1}^{M} c_j f(e|0, \dots, c_j, \dots, 0), \qquad (12)$$

where $f(e|0, \dots, c_j, \dots, 0)$ is a conditional distribution of the signal from a single j^{th} FVE (while the stopping power in the rest of the sample keep fixed). In these notations Fig. 4c corresponds to normalized concentration $\mathbf{c}$ and Fig. 4a shows $f(e|0, \dots, c_j, \dots, 0)$. Fig. 5a represents $c_j f(e|0, \dots, c_j, \dots, 0)$, while Fig. 5c gives $f(e|\mathbf{c})$. The distribution of particles at the exit of the battery stack can then be simulated. For example, the spectrum,

corresponding to the charged battery state at cycle 100, is presented in Fig. 6. The simulated spectrum (pink line, solid and dash) is compared with the experimentally measured spectra for both the alpha particles (blue) and tritons (cyan), indicating good agreement between the theoretically predicted and measured energy profiles. The final simulated spectrum has been corrected for spectrometer resolution 35 keV, while the experimentally observed spectrum was subject to background subtraction and subsequent smoothing. One can see good agreement between the measured and simulated spectra for both types of particles.

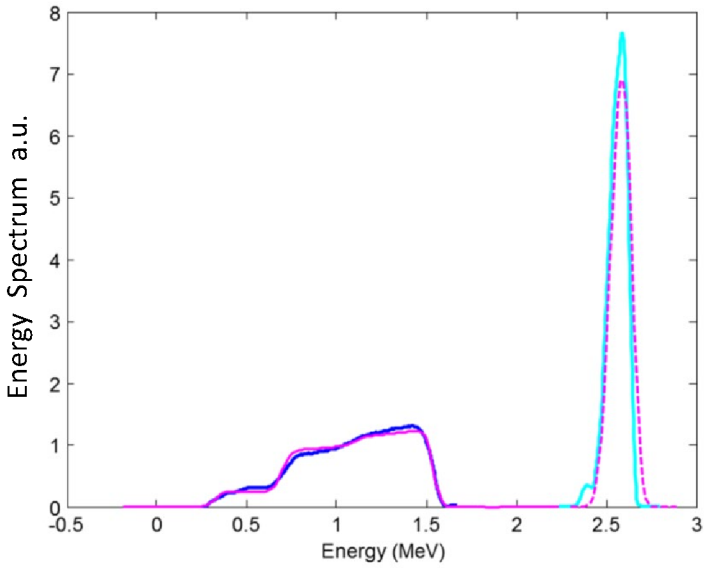

Fig. 6. Comparison of a theoretical (pink, solid and dash line) and experimentally measured spectrum of alpha particles (blue) and tritons (cyan).

Consider a conditional distribution $f(e|0,\dots,c_j,\dots,0)$. An expected value for this conditional distribution is given by

$$\overline{E}_j = \int e f(e|0,\dots,c_j,\dots,0)de \ , \qquad (13)$$

where $\overline{E}_j$ represents an average value of the energy of the particles coming from j^{th} FVE. Define an Energy-Depth calibration function for the thin-film sample, according to

$$D_E(\overline{E}_j) = d_j \, , \qquad (14)$$

where d_j is the location coordinate for the middle of j^{th} FVE layer. Eq. 14 defines the value of the function in point $\overline{E}_j$ equal to d_j. Then, for an arbitrary E, function $D_E(E)$ is

defined by linear interpolation from the table given by Eq. 14. The function $D_E(E)$ for the solid-state battery is shown in Fig. 7, considering the alpha particles in the 200th FVE. Note that Fig. 7 is in good qualitative agreement with Fig. 1, where $LiCoO_2$ was shown to have the largest stopping power and therefore produces the smallest slope in Fig. 7.

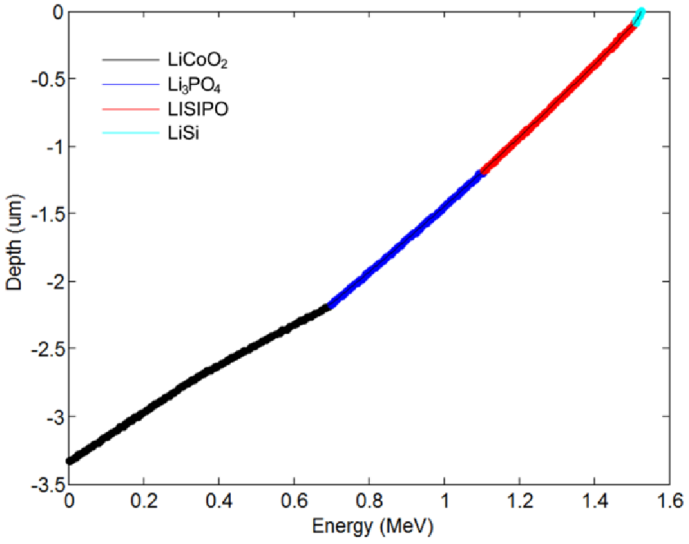

Fig. 7. Energy-Depth calibration function.

According to the calibration function, each point in the observed energy spectrum can be related to certain depth by applying $D_E(E)$. That gives the approximate depth from which this part of the spectrum came from. The second part of the depth profile algorithm is an estimator of the amount of lithium at that particular depth. Denote $\hat{f}(E)$ of the observed NDP spectrum at energy E, *i.e.* the experimentally measured analog at the left-hand side of Eq. 12. Then the Bayesian estimates [31] for normalized Li concentration at depth $D_E(E)$ is written as $\hat{c}(E) = k_n \frac{\hat{f}(E)}{dD_E(E)/dE}$, where the derivative $dD_E(E)/dE$ is obtained by numerical differentiation of the calibration function $D_E(E)$, see Fig. 7 and normalization constant k_n is obtained from the condition $\int_0^\infty \hat{c}(E)dE = 1$. From Bayesian perspective $\hat{f}(E)$ represents 'a data', while multiplier $\frac{k_n}{dD_E(E)/dE}$ is 'a prior'. A pair of

$$\left[D_E(E), k_n \frac{\hat{f}(E)}{dD_E(E)/dE}\right] \quad (15)$$

represents an NDP estimate for normalized lithium concentration in the experimentally measured sample. A corresponding numeric illustration can be found in Fig. 8b which

shows a comparison with the known theoretical distribution of lithium given by the three horizontal lines. For that figure $\hat{f}(E)$ was taken to be the simulated distribution of alpha particles from Fig. 5c. The expected theoretical distributions of lithium in cobalt-oxide, LPO, LiSiPO, and LiSi are given by the horizontal lines: black, blue, red and cyan, respectively. The thick pink line represents the estimated lithium concentration as a function of depth, while the thin black, blue, red and cyan lines give the estimated contributions of cobalt-oxide, LPO, LiSiPO and LiSi into estimated normalized lithium concentration, respectively. It can be seen that the analyzed lithium concentration (pink line) serves as a good estimate for the expected concentrations of lithium in thin-film all-solid-state batteries.

In real experiments, the exact distribution of lithium in the sample is not known, as well as the exact thickness of the individual layers. In this case, the NDP estimation algorithm runs in three steps. Firstly, the initial (guess) distribution of both lithium and layers thicknesses is estimated by finding the best agreement between the simulated and experimentally measured spectra (Fig. 6). Then on the basis of the SRIM program output, the calibration function is determined and, finally, the NDP estimator is determined, according to Eq. 15.

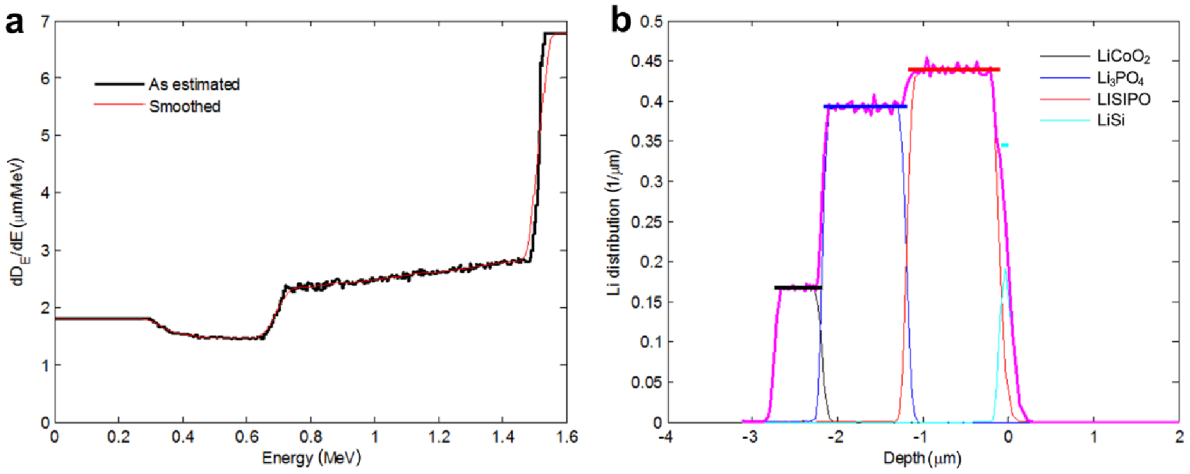

Fig. 8. Derivative of the calibration function $dD_E(E)/dE$ (a). Simulated Li concentration profile compared to the theoretically expected Li distribution, corresponding to Fig. 4c (b).

5. Application to the aging characterization

The NDP raw data used for the energy into depth profile conversion are based on

the energy profiles, which have been reported in [17]. Fig. 2a describes such a battery at the charged state after cycling when a LiSiPO interlayer, which has a chemical composition of $Li_{3+\beta}Si_{\alpha}PO_4$, has been formed at the anode/electrolyte interface. The following parts can be identified from left to right: $LiCoO_2$ cathode, LPO electrolyte, LiSiPO interlayer, Si anode, Cu current collector and packaging coating.

According to the general battery concept, the $LiCoO_2$ cathode is separated from the Si-based anode by a LPO-type of solid-state electrolyte with the initial chemical composition of Li_3PO_4. When Si migrates into the LPO matrix and gets trapped it can immobilize some additional lithium atoms, according to

$$Li_3PO_4 + \alpha\ Si + \beta\ Li \rightarrow Li_{3+\beta}Si_{\alpha}PO_4. \quad (16)$$

The newly formed interfacial electrolyte with composition $Li_{3+\beta}Si_{\alpha}PO_4$ can be denoted as LiSiPO. The Si anode material fraction that migrates into the LPO layer is defined as z. If the original molar amount of Si in the anode is denoted by n_{Si}, the molar amount of Si migrating into LPO can be represented by $n_{Si:LPO} = z\ n_{Si}$. It is furthermore assumed that the number of Li-atoms stored per Si inside the solid-state electrolyte is constant and is determined by β/α, according to Eq. 16. This ratio and other parameters have been determined from a comparison between the Monte Carlo NDP simulations and the experimentally measured NDP spectra. The as-determined parameter development of a thin film Si-LPO-$LiCoO_2$ battery during cycling is summarized in Table 1. It indicates that the Si migration into LPO only occurs in the charging process and the largest loss of Si electrolyte takes place at the first charging cycle. β/α was found to be up to 10, which is comparable to the compositions reported before [32, 33]. Preparing LiSiPO electrolyte according to this composition should prevent Si migration into the solid electrolyte, and, therefore prevent lithium loss.

On the basis of the above analysis, the energy profiles extensively discussed in [17] have been converted to depth profiles. The resulting depth profiles as a function of cycle number are shown in Fig. 9a and b for the charged and discharged states, respectively. Again it is clear that lithium becomes immobilized in the solid-state electrolyte. In addition, some lithium stays behind in the anode and is therefore no longer available to fully discharge the cathode, but this is mainly related to kinetic limitations as NDP measurements confirm that most of the lithium residue can indeed be further extracted from the Si anode after CCCV discharging (compare the violet and red curve in

Fig. 9a). Strikingly, the Li-accumulation layer in the solid-state electrolyte is still present in the discharged state and is growing upon cycling.

Quantification of these degradation processes can be achieved by the integration of the depth profiles-signal changes in the fully discharged battery states of Fig. 9b for the three individual electrode/electrolyte regions. The integrated, immobilized charge in the solid-state electrolyte $Q_e(n)$, the anode $Q_a(n)$, and the cathode $Q_c(n)$ is a function of cycle number (n) and can be represented by

$$Q_i(n) = \frac{A_i(n)}{A_c(1)} Q_c(1), \qquad (17)$$

where subindex *i* can be e, a and c accordingly. The integrated peak areas of the electrolyte $A_e(n)$, anode $A_a(n)$ and cathode $A_c(n)$ in the discharged battery state during cycling are related to the integrated cathode peak area in the charged battery state in the first cycle $A_c(1)$ and the electrochemical charge introduced during the first charging $Q_c(1)$. The results for the electrolyte and the Si electrode are shown by the red and black curve in Fig. 9c, respectively. The amount of immobilized lithium in the electrolyte region is increasing (green curve). The amount of lithium staying behind in the Si electrode is more or less constant upon cycling (black curve). As this feature has a kinetic origin it is, formally speaking, not related to a battery aging process. The summation of these two lines is represented by the open symbols in Fig. 9c and represents the total loss of lithium upon cycling. The total battery capacity loss $Q_c(n)$, obtained by integration of cathode peak area, is also shown in Fig. 9c (red curve) and the result matches very well with the summation of the two Li-ion loss sources (open blue symbols). The as-determined integrated NDP capacity losses also match very well with the storage capacity decay curve, shown in the inset of Fig. 9d, implying fast degradation during the initial 30 cycles followed by a more slow degradation process at higher cycle numbers.

Table 1. *Optimized battery parameters as a function of cycle number.*

Symbol	z	α	β
Definition	Cumulative fraction of Si migrated into LPO	Atomic amount of Si per LPO in LiSiPO	Excess atomic amount of Li per LPO in LiSiPO
Remark/applicability	Growing upon cycling	Growing, reflecting the fact that LiSiPO becomes more Si-rich during aging	Growing, reflecting the fact that more Li is trapped in LISIPO during aging
1^{st} charge	0.160	0.035	0.35
1^{st} discharge	0.160	0.035	0.35
2^{nd} charge	0.160	0.035	0.35
2^{nd} discharge	0.160	0.035	0.35
10^{th} charge	0.220	0.038	0.38
10^{th} discharge	0.220	0.038	0.38
100^{th} charge	0.260	0.044	0.44
100^{th} discharge	0.260	0.044	0.44
250^{th} charge	0.300	0.048	0.48
250^{th} discharge	0.300	0.048	0.48

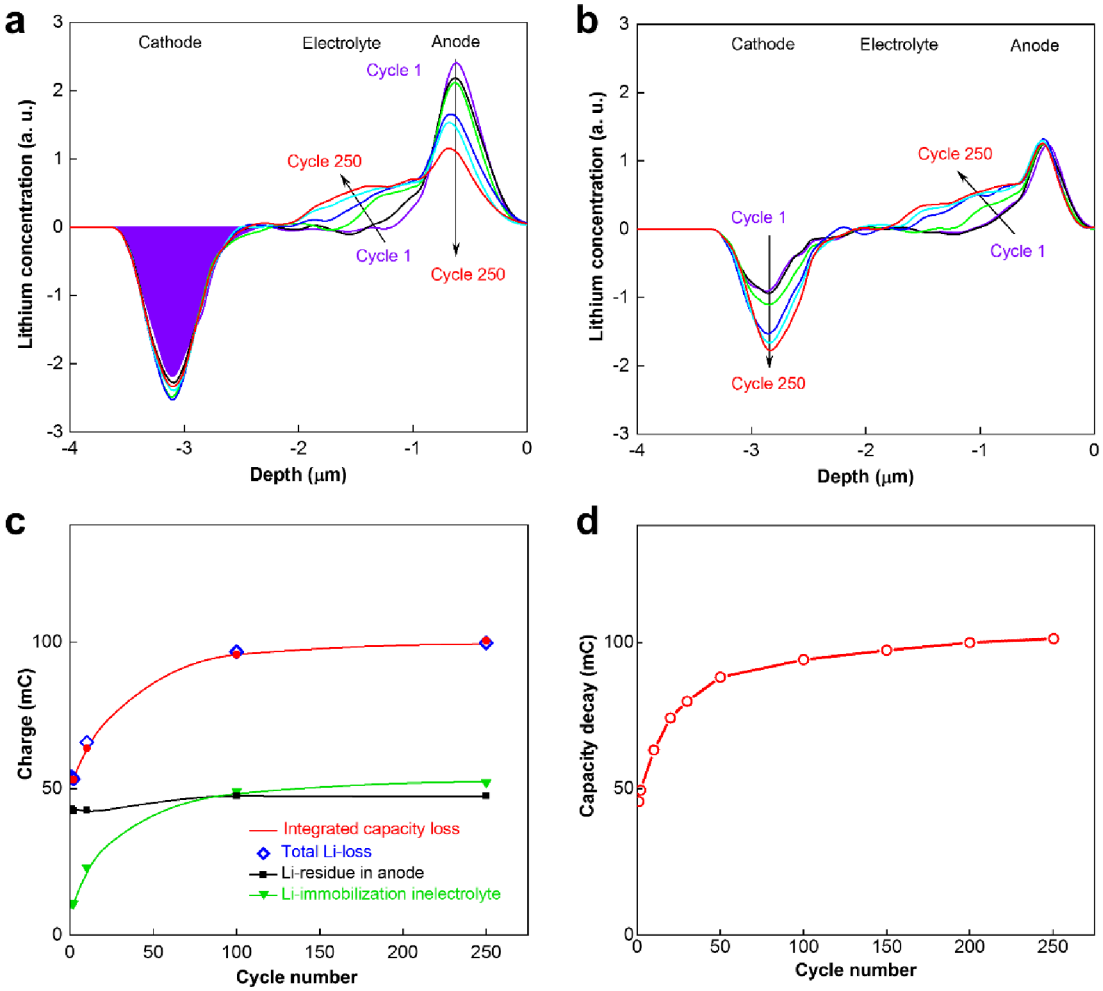

Fig. 9. As-calculated depth profiles of the normalized lithium concentration at the charged (a) and discharged (b) state in the 1st (violet), 2nd (black), 10th (green), 30th (blue), 100th (cyan) and 250th (red) cycle for which the signal of the pristine (discharged) battery has been subtracted. Integrated NDP curves of the discharged battery shown as a function of cycle number (c). The green curve represents the integrated capacity loss due to lithium immobilization in the solid-state electrolyte $Q_e(n)$ and the black curve shows the integrated lithium residue in the Si anode $Q_a(n)$. The open blue symbols show the summation of the integrated signals of the electrolyte and Si anode, which agrees very well with the red curve, representing the integrated capacity reduction of the cathode $Q_c(n)$. Capacity fade of complete battery (d).

Conclusions

It has been demonstrated that the presented Monte Carlo model in combination with available SRIM/TRIM software can be employed to successfully convert NDP energy profiles to lithium concentration depth profiles. In the SRIM/TRIM Monte Carlo calculations, the stopping power of the generated particles in NDP is mainly based on the

interactions with the electronic clouds other than the nuclei of the material atoms. For the energy-to-depth conversion, the full battery has been discretized into finite volume elements to simulate a source of alpha particles and tritons. The simulated spectra have been compared with the experimentally measured spectra. Optimal thicknesses of battery stack layers were obtained by minimizing the discrepancy between the simulated and measured spectra. The relation between the average energy of alpha particles emitted by particular FVE and the depth of the corresponding FVE was used to relate the particular energy of the spectrum with the depth where the emitting source is located. Finally, a Bayesian estimator was applied to calculate the distribution of lithium at a particular depth.

The developed depth profile estimation method was applied to simulate a reference spectrum of a battery stack of known materials and thicknesses. It was found that the method can reveal the known lithium distribution with a good degree of accuracy. Subsequently, the depth profile estimation method was applied to experimental data reported in [17]. It is shown that the process of lithium accumulation in the LPO electrolyte can be elegantly unraveled and was shown to be the origin of the aging of all-solid-state thin-film Li-ion batteries. The so-called difference depth profiles have been used to quantify the degree of lithium immobilization in the electrolyte, which matches very well with the measured electrochemical results.

References

[1] Renewables 2018 Global Status Report, A comprehensive annual overview of the state of renewable energy, http://www.ren21.net/gsr-2018/.

[2] Plugged in: The end of the oil age, World Wide Fund for Nature 2008, *assets.panda.org/downloads/plugged_in_full_report___final.pdf.*

[3] P.P.R.M.L. Harks, F.M. Mulder, P.H.L. Notten, In situ methods for Li-ion battery research: A review of recent developments. J. Power Sources 2015, 288, 92-105.

[4] J.F. Ziegler, G.W. Cole, J.E.E. Baglin, Technique for determining concentration profiles of boron impurities in substrates, J.Appl.Phys., 43, 3809 (1972).

[5] J.P. Biersack, D. Fink, Observation of the blocking effect after 6Li(n, t) 4He reactions with thermal neutrons, Nuclear Instruments and Methods 108, 397-399, (1973)

[6] K. Mueller, R. Henkelmann, H. Boroffka, The determination of low dose boron implanted concentration profiles in silicon by the (n,α) reaction, Nuclear Instruments and Methods, 128, 557-559, 1975

[7] J. Cervena, V. Hnatowicz, J. Hoffmann, Z. Kosina, J. Kvitek, P. Onheiser, Nucl Instr Meth 188, 185-189, 1981

[8] R.G. Downing, R.F. Fleming, J.K. Langland, D.H. Vincent, Neutron depth profiling at the National Bureau of Standards, Nucl. Instr. Meth 218, 47-51, 1983

[9] L.H.M. Krings, Y. Tamminga, J. van Berkum, F. Labohm, A. van Veen, W.M. Arnoldbik, Lithium depth profiling in thin electrochromic WO3 films. J. Vac. Sci. Technol. A 1999, 17, 198-205.

[10] G.P. Lamaze, H. Chen-Mayer, M. Badding, M.L. Laby, In-situ measurement of lithium movement in thin film electrochromic coatings using cold neutron depth profiling. Surf. Interface Anal. 1999, 27, 644-647.

[11] G.P. Lamaze, H.H. Chen-Mayer, A. Gerouki, R.B. Goldner, Analysis of lithium transport in electrochromic multilayer films by neutron depth profiling. Surf. Interface Anal. 2000, 29, 638-642.

[12] G.P. Lamaze, H.H. Chen-Mayer, D.A. Becker, F. Vereda, R.B. Goldner, T. Haas, P. Zerigian, Cold neutron depth profiling of lithium-ion battery materials. J. Power Sources 2003, 119-121, 680-685.

[13] R.G. Downing, G.P. Lamaze, J.K. Langland, S.T. Hwang, Neutron depth profiling: overview and description of NIST facilities. J. Res. Natl. Inst. Stand. Technol. 1993, 98, 109-126.

[14] D. X. Liu, J.H. Wang, K. Pan, J. Qiu, M. Canova, L.R. Cao, A.C. Co, In situ quantification and visualization of lithium transport with neutrons. Angew. Chem. Int. Ed. 2014, 53, 9498-9502.

[15] X.Y. Zhang, T.W. Verhallen, F. Labohm, M. Wagemaker, Direct observation of Li-ion transport in electrodes under nonequilibrium conditions using neutron depth profiling. Adv. Energy Mater. 2015, 1500498 (1-8).

[16] J.F.M. Oudenhoven, F. Labohm, M. Mulder, R.A.H. Niessen, F.M. Mulder, and P.H.L. Notten, In situ neutron depth profiling: A powerful method to probe lithium transport in micro-batteries. Adv. Mater. 2011, 23, 4103-4106.

[17] C.G. Chen, J.F.M. Oudenhoven, D L. Danilov, E. Vezhlev, L. Gao, N. Li, F. M. Mulder, R.-A. Eichel, P.H.L. Notten, *Advanced Energy Materials*, **8** (2018) 201801430 (1-11), DOI: 10.1002/aenm.201801430.

[18] http://www.srim.org/

[19] N. Bohr, On the constitution of atoms and molecules, *Philos. Mag.* **1913**, 25, 10.

[20] N. Bohr, On the decrease of velocity of swiftly moving electrified particles in passing through matter, *Philos. Mag.* **1915**, 30, 581.

[21] H. Bethe, Zur Theorie des Durchgangs schneller Korpuskularstrahlen durch Materie, *Ann. Phys.* **1930,** 5, 325.

[22] H. Bethe, Bremsformel für Elektronen relativistischer Geschwindigkeit, *Z. Phys.* **1932,** 76, 293.

[23] F. Bloch, Durchgang schneller Korpuskularstrahlen durch ein Ferromagnetikum, *Ann. Phys.* **1933,** 16, 285.

[24] F. Bloch, Bremsvermögen von Atomen mit mehreren Elektronen, *Z. Phys.* 1933, 81, 363.

[25] U. Fano, Penetration of Protons, Alpha Particles, and Mesons, *Annu. Rev. Nucl. Sci.* **1963**,13, 1.

[26] U. Fano, Studies in Penetration of Charged Particles in Matter, Nuclear Science Report No. 39, U.S. National Academy of Sciences, Washington DC, 1964, 1–338.

[27] L.C. Northcliff, Phys. Rev. **1960**, 120, 1744.

[28] H.O. Wyckoff, ICRU Scientific Counsellor, 'Stopping Powers and Ranges for Protons and Alpha Particles, Intl. Comm. on Rad. Units, Bethseda, MD, 1993, ICRU-49.

[29] J. F. Ziegler, J. P. Biersack,and U. Littmark, The Stopping and Range of Ions in Solids, Pergamon Press, New York **1985**.

[30] J.F. Ziegler, Stopping of energetic light ions in elemental matter. *J. Appl. Phys*. **1999**, *85*,

1249-1272.

[31] J.O. Berger, Statistical Decision Theory and Bayesian Analysis, Springer, New York **1985**.

[32] Y.R. Su, J. Falgenhauer, T. Leichtweiβ, M. Geiβ, C. Lupó, A. Polity, S.Q. Zhou, J. Obel, D. Schlettwein, J. Janek, B.K. Meyer, Electrochemical properties and optical transmission of high Li^+ conducting LiSiPON electrolyte films, *Phys. Status Solidi B* **2017**, *254*, 1600088 (1-8).

[33] M. Aslam, X.Y, Kong, A lithium ion conductor in Li_4SiO_4-Li_3PO_4-$LiBO_2$ ternary system. *Solid State Ionics* **2016**, *293*, 72-76.